Memory-assisted quantum accelerometer with multi-bandwidth

Zhifei Yu,[1] Bo Fang,[1] Liqing Chen,[1,2,*] Keye Zhang,[1] Chun-Hua Yuan,[1,2,5] and Weiping Zhang[2,3,4,6]

[1]State Key Laboratory of Precision Spectroscopy, School of Physics and Electronic Science, East China Normal University, Shanghai 200062, China
[2]Shanghai Research Center for Quantum Sciences, Shanghai 201315, China
[3]School of Physics and Astronomy, Shanghai Jiao Tong University, and Tsung-Dao Lee Institute, Shanghai 200240, China
[4]Collaborative Innovation Center of Extreme Optics, Shanxi University, Taiyuan 030006, China
[5]e-mail: chyuan@phy.ecnu.edu.cn
[6]e-mail: wpzhang@phy.ecnu.edu.cn
*Corresponding author: lqchen@phy.ecnu.edu.cn

The accelerometer plays a crucial role in inertial navigation. The performance of conventional accelerometers such as lasers is usually limited by the sensing elements and shot noise limitation (SNL). Here, we propose an advanced development of an accelerometer based on atom–light quantum correlation, which is composed of a cold atomic ensemble, light beams, and an atomic vapor cell. The cold atomic ensemble, prepared in a magneto-optical trap and free-falling in a vacuum chamber, interacts with light beams to generate atom–light quantum correlation. The atomic vapor cell is used as both a memory element storing the correlated photons emitted from cold atoms and a bandwidth controller through the control of free evolution time. Instead of using a conventional sensing element, the proposed accelerometer employs interference between quantum-correlated atoms and light to measure acceleration. Sensitivity below SNL can be achieved due to atom–light quantum correlation, even in the presence of optical loss and atomic decoherence. Sensitivity can be achieved at the ng/$\sqrt{\text{Hz}}$ level, based on evaluation via practical experimental conditions. The present design has a number of significant advantages over conventional accelerometers such as SNL-broken sensitivity, broad bandwidth from a few hundred Hz to near MHz, and avoidance of the technical restrictions of conventional sensing elements. © 2022 Chinese Laser Press

https://doi.org/10.1364/PRJ.453940

1. INTRODUCTION

Accelerometers have extensively been applied as weak force probes, especially in situations that involve inertial navigation, land-based resource exploration, and seismic monitoring [1–4]. There are many types of accelerometers, including capacitive [5,6], piezoelectric [7], tunnel-current [8], thermal [9], and optical [10–16]. Almost all utilize mass-spring-damper systems as displacement sensors [17]. The performance of such accelerometers highly relies on fabrication of the displacement sensors, which directly results in technical limitations to the bandwidth, quality factor Q_f, and noise level [18]. Among numerous accelerometers, optical ones have attracted much attention due to their high sensitivity. However, the sensitivity of such accelerometers is fundamentally subject to shot noise limitation (SNL) [19,20]. Developing methods and technologies to break the SNL and remove the technical limitations of conventional displacement sensors is desired for the innovation of accelerometers.

In this paper, we present a memory-assisted quantum accelerometer (MQA), which consists of atomic ensembles, light beams, and optical elements. The MQA has three advantages over conventional accelerometers. First, instead of a mass-spring-damper system, a cold atomic ensemble [21] acts as the displacement sensor, which can avoid the technical restrictions of a mass-spring-damper system. Second, the SNL-broken sensitivity in measurement of acceleration can be achieved by the quantum interference of correlated atoms and light [22–24]. The third merit is that the accelerometer allows a tunable bandwidth, which is determined by the controllable memory time t_M of the correlated photons stored in a memory element [25–27]. We calculate and analyze the sensitivity and bandwidth of the MQA. An inverse relation exists between sensitivity and bandwidth. Sensitivity can reach below the SNL in the range of bandwidth from a few hundred Hz to near MHz due to atom–light quantum correlation, even in the presence of the optical losses and atomic decoherence.

An optimal ng/$\sqrt{Hz}$-level sensitivity without loss is anticipated at frequencies ~100 Hz for a feasible average atomic number and an available memory time $t_M = 10$ ms.

2. RESULTS

A. Principle of MQA

A schematic diagram of the accelerometer is shown in Fig. 1. The cores are composed of two atomic systems: cold ensemble A_1 and atomic vapor cell A_2. A_1 is prepared in a magneto-optical trap (MOT), free-falling in the vacuum chamber to generate atom $(\hat{S}_{a_1}^{(1)})$–light $(\hat{a}_1)$ quantum correlation and realize atom–light interference via two Raman scattering processes. Atomic vapor cell A_2, containing thermal atoms and buffer gas, is a memory element to store the correlated photonic signal $\hat{a}_1$ from A_1, which acts as a bandwidth modulator. In principle, the memory element can be any quantum memorizer for
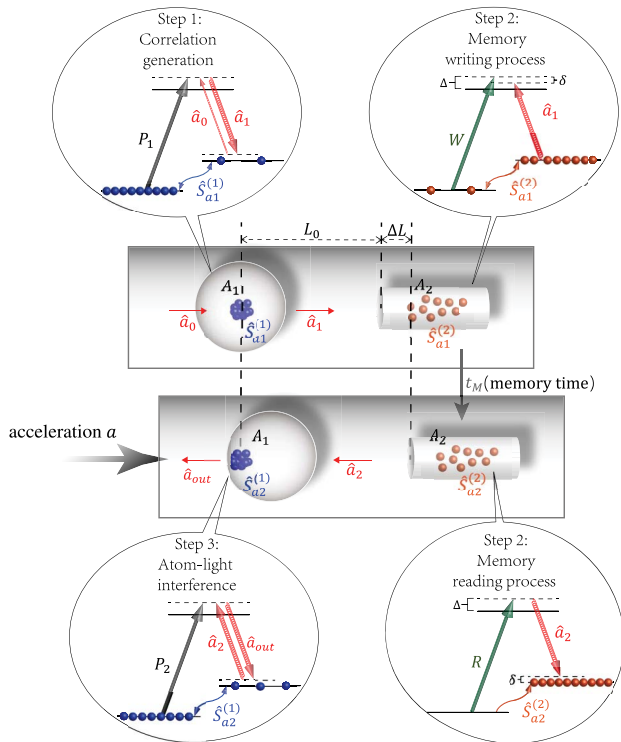
Fig. 1. Schematic diagram of the MQA. The cold atomic ensemble A_1 is free-falling in the vacuum chamber. Atomic vapor A_2, the vacuum chamber, and all optical elements are fixed on and move with the platform at acceleration a. The distance between A_1 and A_2 is changed from L_0 to $L_0 + \Delta L$. ΔL is the acceleration-dependent displacement achieved via atom–light quantum interference, which is realized in three steps. Step 1: $\hat{a}_1$ and $\hat{S}_{a_1}^{(1)}$ are generated by the first stimulated Raman scattering (SRS) in A_1 via input seed $\hat{a}_0$ and Raman pump P_1. The atomic spin wave is $\hat{S}_{a_j}^{(i)}$, where superscript i ($i = 1, 2$) indicates different atomic ensemble A_1 or A_2, and subscript j ($j = 1, 2, 3$) represents the evolution state at different times of atomic ensemble A_i. Step 2: $\hat{a}_1$ is stored in A_2 as $\hat{S}_{a_1}^{(2)}$ is driven by the strong write pulse W. After memory time t_M, $\hat{S}_{a_2}^{(2)}$, evolved from $\hat{S}_{a_1}^{(2)}$ due to atomic decay, is retrieved back to $\hat{a}_2$ by the read pulse R. Step 3: $\hat{S}_{a_2}^{(1)}$, evolved from $\hat{S}_{a_1}^{(1)}$ during the memory time, and $\hat{a}_2$ interfere by the second SRS via Raman pump P_2.

photons with long coherence times, such as rare-earth-doped crystals [28,29]. All optical devices including the vacuum chamber and memory element are fixed onto a mobile platform. When MOT is turned on, A_1 and A_2 move together with the platform. The distance L between two atomic systems is fixed as L_0 at any velocity or acceleration of the platform. When MOT is turned off, A_1 is free-falling in vacuum, acting as the static frame reference, and A_2 remains moving with the platform at acceleration a. $L = L_0 + \Delta L$ changes with acceleration, where ΔL is the displacement due to acceleration a. $\Delta L = \frac{1}{2} a T^2$, where T is the free-evolution time duration after the first Raman scattering process and before the second one, that is, the atom–light "wave-splitting" and "wave-recombining" processes, respectively. T is independent of acceleration a and the velocity of the platform. ΔL can be achieved via atom–light quantum interference. Acceleration a can be achieved by the variation of ΔL with time T. The acceleration sensitivity is no longer limited by the performance of the mass-spring-damper system. This is one of the advantages of our scheme.

The accelerometer is operated in three steps: generation of atom–light quantum correlation via the first Raman scattering in A_1, atomic memory in A_2, and acceleration acquisition via atom–light interference. Below, we describe the calculation and analysis in detail.

B. Generation of Quantum Correlation

Atom–light quantum correlation is generated via stimulated Raman scattering (SRS) in A_1, which is effectively an atom–light wave-splitting process. A Stokes seed $\hat{a}_0$ and a strong Raman beam P_1 interact with the atoms in A_1 to generate Stokes light $\hat{a}_1$ and atomic spin wave $\hat{S}_{a_1}^{(1)}$ [30]. The input–output relation of SRS can be written as $\hat{a}_1 = G_1 \hat{a}_0 + g_1 \hat{S}_{a_0}^{(1)\dagger} e^{i\theta_{P_1}}$, $\hat{S}_{a_1}^{(1)} = G_1 \hat{S}_{a_0}^{(1)} + g_1 \hat{a}_0^\dagger e^{i\theta_{P_1}}$. $\hat{S}_{a_0}^{(1)}$ describes the initial spin wave, which starts from the ground state of the atomic ensemble. G_1 and g_1 are Raman gains that satisfy $G_1^2 = g_1^2 + 1$, and θ_{P_1} is the phase of beam P_1.

After SRS, the generated Stokes signal $\hat{a}_1$, transmitting out of A_1 and entering A_2, quantum-mechanically correlates with the induced atomic spin wave $\hat{S}_{a_1}^{(1)}$ that remains in A_1. The intensity fluctuations of both $\hat{a}_1$ and $\hat{S}_{a_1}^{(1)}$ are amplified to the level above SNL as a result of Raman amplification. But the relative intensity fluctuation $\hat{S}_{a_1}^{(1)\dagger} \hat{S}_{a_1}^{(1)} - \hat{a}_1^\dagger \hat{a}_1$ is squeezed below SNL by $2G_1^2 - 1$ times, due to the quantum correlation between $\hat{a}_1$ and $\hat{S}_{a_1}^{(1)}$ (see Appendix A).

C. Atomic Memory

Stokes signal $\hat{a}_1$ propagates into atomic vapor cell A_2, and then is stored as atomic spin wave $\hat{S}_{a_1}^{(2)}$ in the writing process driven by the write beam W. The evolution of the spin wave obeys the Heisenberg propagation equation

$$\frac{\partial}{\partial t} \hat{S}_{a_1}^{(2)} = -i \left(\frac{|\Omega_W|^2}{\Delta} - \delta + \Delta \mathbf{k}_W \cdot \mathbf{v} \right) \hat{S}_{a_1}^{(2)} - i \chi \hat{a}_1, \quad (1)$$

where Ω_W is the Rabi frequency of W, Δ is single-photon detuning, δ is two-photon detuning, $\Delta \mathbf{k}_W = \mathbf{k_W} - \mathbf{k_s}$ is the wave vector difference of W and $\hat{a}_1$, χ is the Raman coupling coefficient, $\mathbf{v}$ is the center of mass velocity of the atoms, and

$\Delta\mathbf{k}_W \cdot \mathbf{v}$ is the Doppler frequency shift. The solution to Eq. (1) is (see Appendix B)

$$\hat{S}_{a_1}^{(2)} = (-i\sqrt{\eta_W}e^{i\theta_W}\hat{a}_1 e^{i\varphi} + e^{i\theta_{W_0}}\sqrt{1-\eta_W}\hat{S}_{a_0}^{(2)})$$
$$\times e^{-i\left(\frac{|\Omega_W|^2}{\Delta}-\delta+\Delta\mathbf{k}_W\cdot\mathbf{v}\right)t_W/2}, \qquad (2)$$

where η_W is the writing efficiency determined by the coupling coefficient χ; $\varphi = k_s L_0$, and $k_s = 2\pi/\lambda_s$, with λ_s the Stokes wavelength. θ_W is the phase of the write field W; t_W is the writing time. $\hat{S}_{a_0}^{(2)}$ is the initial spin wave in A_2, which is in the vacuum state. The term $\frac{|\Omega_W|^2}{\Delta}$ corresponds to the Stark effect. $\frac{|\Omega_W|^2}{\Delta}$, δ, and θ_{W_0} are acceleration-independent parameters, which can be considered as fixed values.

After memory time t_M, $\hat{S}_{a_2}^{(2)}$, evolving from $\hat{S}_{a_1}^{(2)}$ with decay rate Γ_2 due to atomic collisions, can be read out as Stokes $\hat{a}_2$ with efficiency η_R by the read beam R. Assuming a reading time $t_R \sim t_W$ and defining $\eta = \eta_W \eta_R$, Stokes $\hat{a}_2$ can be simplified as (see Appendix C)

$$\hat{a}_2 = -\sqrt{\eta}e^{-i(\Delta\varphi_a+\Delta\varphi_v-\varphi_0)}e^{-\Gamma_2 t_M}\hat{a}_1 + \sqrt{1-\eta e^{-2\Gamma_2 t_M}}\hat{V}, \qquad (3)$$

where $\hat{V}$ is the effective vacuum field. The phase offset φ_0 can be safely set to zero since it is independent of the measured acceleration a (see Appendix C). The velocity-dependent phase shift $\Delta\varphi_v = \Delta\mathbf{k}_W \cdot \mathbf{v}t_M$ is induced by the Doppler effect due to the center of mass motion of atoms. The acceleration-dependent phase shift $\Delta\varphi_a \equiv \Delta k a t_M(t_M - t_W)/2 - k_s(\Delta L)$, where Δk is the projection of $\Delta\mathbf{k}_W$ along the acceleration. $\Delta L = \frac{1}{2}aT^2 = \frac{1}{2}a(t_1 + t_2 + t_M)^2$, where t_1 and t_2 are the flying times of the Stokes light between cold ensemble A_1 and vapor cell A_2 forth and back, respectively. Normally, $k_s \gg |\Delta k|$ and $t_M \gg t_{W,R} \gg t_{1,2}$, i.e., $\Delta\varphi_a \simeq -k_s a t_M^2/2$. The phase shift of the Stokes field can be measured through atom–light interference between the readout field $\hat{a}_2$ returning to A_1 and atomic spin wave $\hat{S}_{a_1}^{(1)}$ remaining in A_1.

D. Atom–Light Interference

When a_2 returns to A_1, the atomic spin wave $\hat{S}_{a_1}^{(1)}$ has experienced free evolution for the duration of memory time t_M. As a result, the spin wave has the form $\hat{S}_{a_2}^{(1)} = \hat{S}_{a_1}^{(1)}e^{-\Gamma_1 t_M} + \hat{F}^{(1)}$, with Doppler dephasing being negligible in the cold ensemble (see Appendix D), where $\hat{F}^{(1)}$ is the quantum Langevin operator, reflecting the collision-induced fluctuation and satisfying $[\hat{F}^{(1)}, \hat{F}^{(1)\dagger}] = 1 - e^{-2\Gamma_1 t_M}$ [24]. The decay rate Γ_1 represents the decoherence effect due to atomic collisions and flying off the laser beam. For a general cold atomic ensemble, the root mean square velocity is $\sim$ several cm/s, and the diffusion of cold atoms is $\sim$1.0 mm after a memory time of 10 ms. The whole atomic ensemble will drop 0.5 mm in gravity direction after 10 ms. The mismatch of the spot expansion and dropping of the cold atomic ensemble plays an opposite role in quantum enhancement by destroying atom–light quantum correlation. However, these two effects can be solved using laser beam expansion and light path adjustment in the experiment.

$\hat{a}_2$ and $\hat{S}_{a_2}^{(1)}$ interact with each other in A_1, which is driven by P_2 with $\theta_{P_2} = \theta_{P_1}$, and generate Stokes $\hat{a}_{\mathrm{out}}$ with atomic spin wave $\hat{S}_{a_{\mathrm{out}}}^{(1)}$ by a second Raman scattering. Setting $\sqrt{T_1} \equiv e^{-\Gamma_1 t_M}$ and $\sqrt{T_2} \equiv e^{-\Gamma_2 t_M}$, we have the

final output $\hat{a}_{\mathrm{out}} = \varsigma_1\hat{a}_0 + \varsigma_2\hat{S}_{a_0}^{(1)\dagger} + \varsigma_3\hat{V} + \varsigma_4\hat{f}^\dagger$ (see Appendix D), where $\hat{f}$ is the normalized noise operator, $\hat{f} \equiv \hat{F}^{(1)}/\sqrt{1-T_1}$, $\varsigma_1 \equiv g_1 g_2\sqrt{T_1} - G_1 G_2\sqrt{\eta T_2}e^{i(\Delta\varphi_a+\Delta\varphi_v)}$, $\varsigma_2 \equiv e^{i\theta_{P_2}}[G_1 g_2\sqrt{T_1} - g_1 G_2\sqrt{\eta T_2}e^{i(\Delta\varphi_a+\Delta\varphi_v)}]$, $\varsigma_3 \equiv G_2\sqrt{1-\eta T_2}$, and $\varsigma_4 \equiv g_2 e^{i\theta_{P_2}}\sqrt{1-T_1}$.

Here, we emphasize that atomic vapor cell A_2 moves with the platform. To achieve acceleration, this requires that the vapor atoms and cell wall move as a whole, which implies that a robust thermal equilibrium between the atoms and the cell wall is essential during memory time. This is realized with the assistance of buffer gas in the vapor cell. In a room-temperature cell with buffer gas at several-Torr pressure, the mean free path of atoms is $\sim\mu$m, with $v_{\mathrm{rms}} \sim 300$ m/s. This allows the vapor atoms to remain in thermal equilibrium with the cell wall under acceleration (see Appendix D). The ground-state coherence can be preserved for up to 10^8 collisions between the buffer gas and atoms [31]. The buffer gas can separate atoms and decrease the collision between them. Therefore, the value of the decay rate Γ_2 is small [32]. Doppler dephasing ($\Delta\varphi_v$) can be avoided by adopting near-degenerate Zeeman two-photon transitions, as shown in Appendix E. Now the Stokes field $\hat{a}_{\mathrm{out}}$, containing only phase $\Delta\varphi_a$, can be measured through homodyne detection (HD).

E. Acquisition of Acceleration

All optical devices including the vacuum chamber and memory element are fixed onto a mobile platform. When MOT is turned on, cold ensemble A_1 and atomic vapor cell A_2 move together with the platform. The distance L between two atomic systems is fixed as L_0 at any velocity v_0 or acceleration of platform a. When MOT is turned off, the movement of the cold atomic ensemble is independent of the platform. The cold atomic ensemble moves in uniform motion with constant velocity v_0. The atomic vapor still moves with the platform under acceleration. Its velocity changes with acceleration, and the distance between two atomic systems also changes from L_0 to $L_0 + \Delta L$, where $\Delta L = \Delta v_0 T + \frac{1}{2}aT^2$ is the displacement due to acceleration, with Δv_0 the initial relative velocity of A_1 and A_2, and T is independent of the acceleration a and velocity of the platform. ΔL causes a phase shift. Here, Δv_0 is zero because the velocities of two atomic systems are the same before MOT is turned off. Acceleration can be measured in the direction of the seed and pump fields passing the cold ensemble, and it can be expressed in terms of the phase $\Delta\varphi_a$ as follows:

$$a = \frac{\lambda_s \Delta\varphi_a}{\pi t_M^2}. \qquad (4)$$

Using the HD of the quadrature of Stokes field $\hat{a}_{\mathrm{out}}$, acceleration is measured, and sensitivity is given by (see Appendix E)

$$\Delta a = \frac{1}{Q_e}\Delta a_{\mathrm{SNL}}, \qquad (5)$$

where Q_e is the quantum enhancement factor. Sensitivity breaks the SNL when $Q_e > 1$. In general,

$$Q_e = \frac{2G_1 G_2}{\sqrt{G_1^2 + g_1^2}}\frac{\sqrt{\eta}e^{-\Gamma_2 t_M}}{\sqrt{\sum_{n=1}^4 |\varsigma_n^0|^2}}, \qquad (6)$$

where ς_n^0 are the values of ς_n ($n = 1, ..., 4$) at the dark fringe. Defining $N_0 \equiv \langle \hat{a}_0^\dagger \hat{a}_0 \rangle$ for the input mean photon number, we work out the SNL for acceleration measurement:
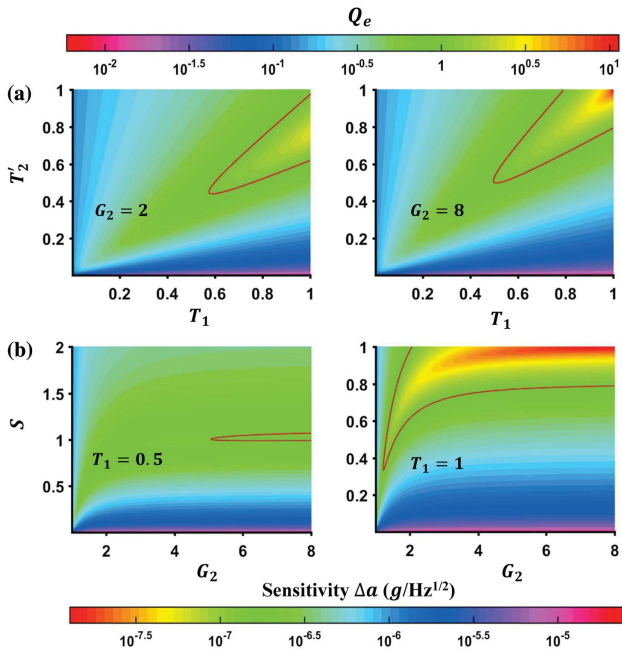
$$\Delta a_{\mathrm{SNL}} = \frac{\lambda_s}{\pi \sqrt{(G_1^2 N_0 + g_1^2 N_0) t_M^2}}, \qquad (7)$$

where $G_1^2 N_0$ and $g_1^2 N_0$ are the particle numbers of Stokes signal $\hat{a}_1$ and atomic spin wave $\hat{S}_{a_1}^{(1)}$, respectively. Acceleration sensitivity depends on the phase sensitivity of atom–light interference, whose SNL is determined by the total phase-sensitive particle number $(G_1^2 + g_1^2) N_0$ of two interference beams, signal $\hat{a}_1$ and atomic spin wave $\hat{S}_{a_1}^{(1)}$. Here, quantum correlation between $\hat{S}_{a_1}^{(1)}$ and $\hat{a}_1$ is key to breaking the SNL in acceleration sensitivity.

F. Accelerometer Sensitivity

To obtain the best sensitivity in the acceleration measurement, it is essential to decrease Δa_{SNL} itself and increase quantum enhancement factor Q_e. In general, Δa_{SNL} can be reduced by increasing the input particle number N_0 and prolonging memory time t_M. However, this is usually constrained in realistic experiments. In this sense, quantum enhancement provides just an alternative way to further improve sensitivity through SNL breaking.

Factor Q_e is complicated, and we numerically analyze the behavior of Q_e in Fig. 2(a) as a function of T_1 and T_2' ($T_2' \equiv \eta T_2$) for a different Raman gain G_2 under a given G_1. The larger T_1, T_2', and G_2, the larger Q_e. The red solid curves with $Q_e = 1$ in Fig. 2(a) set a critical boundary of the SNL, which reflects a balance of competition between losses
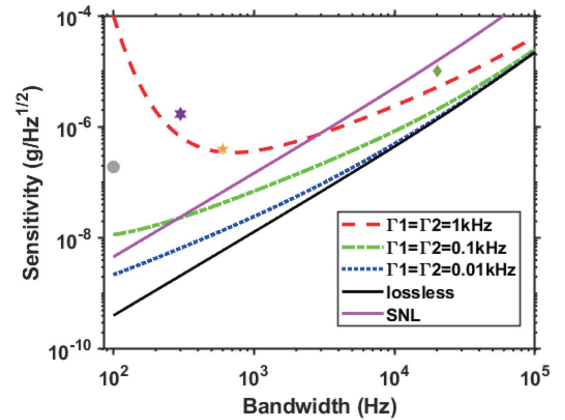
and quantum correlation. The region within the curves marks $Q_e > 1$, representing quantum enhancement.

On the other hand, in terms of Eq. (7), the gains G_1, g_1, and N_0 determine the SNL for acceleration sensitivity. To set an SNL as low as possible in the measurement, it is essential to achieve gains as high as possible. Hence, we assume $G_1 \gg 1$ for numeric analysis. Sensitivity Δa is shown as a function of $s = T_2'/T_1$ and G_2 under given G_1 and N_0 in Fig. 2(b). The quantum enhancing region associated with $Q_e > 1$ is marked as the same within the red solid curves. Obviously, high gain G_2 and low losses can greatly enhance sensitivity due to the sufficient exploitation of quantum correlation. In addition, quantum enhancement of sensitivity well exhibits a loss tolerance, and highly depends on the balance of losses defined by the ratio s. The best sensitivity appears near $s = 1$ for high gains, where the atomic and optical losses are well balanced. In particular, sensitivity can keep beating the SNL through quantum enhancement until losses approach the limit $T_1 \sim T_2' \sim 0.5$.

G. Measurement Bandwidth

Sensitivity Δa is the result determined by one single-shot measurement approximately completed in memory time t_M, which gives the upper limit of the MQA's frequency $f_{\max} = 1/t_M$. In realistic experiments, if the setup of the system takes time t_s, and stable operation for M-times repeating measurements takes time $t_o = M t_M$, then the overall sensitivity of the accelerometer is given by $\Delta a_o \equiv \Delta a / \sqrt{f_{\mathrm{eff}}} \propto (f_{\max})^{3/2}$, where $f_{\mathrm{eff}} = f_{\max} t_o / (t_s + t_o)$.

There is a trade-off between sensitivity Δa_o and bandwidth, as shown in Fig. 3. In general, sensitivity Δa_o has a 3/2 power-law dependence of bandwidth, indicating that sensitivity degrades in the high-frequency region. In Fig. 3, we see that when the losses of the system remain low enough, the accelerometer exhibits well the quantum advantage to achieve an SNL below sensitivity with a broad range of frequencies. Sensitivity rises above the SNL at low frequencies with losses. As a comparison, some available data of sensitivities for previously reported

Fig. 2. (a) Quantum enhancement factor Q_e versus T_1 and T_2' when $G_2 = 2$ and 8, respectively. (b) Sensitivity versus s and G_2 when $T_1 = 0.5$ and 1, respectively. $s = T_2'/T_1$ is the ratio of two beams' losses. The red curves mark $Q_e = 1$ for SNL. Sensitivities within the red curves can beat the SNL. Parameter settings: $N_0 = 10^6$, $G_1 = 8$, $\lambda_s = 795$ nm, and $t_M = 1$ ms.

Fig. 3. Sensitivity as a function of bandwidth under the conditions $G = 8$, $N_0 = 10^6$, $\lambda_s = 795$ nm, and $\eta = 1$. The data of other reported accelerometers are given as comparison. Dark green diamond: microchip optomechanical accelerometer [14]. Orange pentagram: micromechanical capacitive accelerometer [18]. Purple hexagram: MEMS accelerometer [6]. Gray circle: optical accelerometer [15].

accelerometers are labeled in Fig. 3 as well. Overall, the MQA has great potential in highly-sensitive measurements of acceleration.

With the available experimental conditions, e.g., $N_0 = 10^6$ per pulse, Raman gain $G_1 = 8$, $G_2 = 2$, MOT cycle $t_s = 30$ ms [33,34], memory time $t_M \sim 10$ ms [35,36], we can achieve single-shot sensitivity 23 ng at frequency 100 Hz. Finally, the sensitivity is ~ 4.6 ng/$\sqrt{\text{Hz}}$.

For the traditional interferometric accelerometer, the only method to improve sensitivity at a high bandwidth is to increase the quality factor Q_f of the damper, which is technically hard to implement. In our scheme, sensitivity at a high bandwidth can be improved by increasing the Raman gain or the number of initial photons and trapping cold atoms, making it much easier to operate.

3. DISCUSSION AND CONCLUSION

We present an innovative principle for a quantum enhanced accelerometer. There are several significant advantages over other interferometer-based accelerometers: broad bandwidth, SNL below sensitivity, and mechanics-free sensing flexibility compared to mass-spring-damper systems. The dynamic range of acceleration depends on that of phase measurement, which is from the phase sensitivity to 2π. With λ_s of 795 nm, the dynamic range of acceleration of a single shot is from 23 ng to 1.59 mg with $t_M = 10$ ms, and from 2.3 g to 1.59×10^5 g with $t_M = 1.0$ μs. It can be seen that the dynamic range is ~ 48 dB with a fixed t_M. Furthermore, the measurable range of acceleration is from 23 ng to 1.59×10^5 g, ~ 128 dB, only by adjusting t_M to suitable values. In future applications of the MQA, a long atomic coherence time of $A_{1,2}$ and high memory efficiency η are crucial to achieve high sensitivity. Large optical depths for $A_{1,2}$ are required to ensure enough atomic numbers to achieve a large input particle number N_0 and high gains, so as to lower the level of Δa_{SNL} and raise the quantum enhancement factor Q_e.

We emphasize that this work building the MQA is based on quantum correlation. The physics behind this is universal. Hence, the principle presented in this paper is not limited only to the atom–light coupling system, but can be extended to other systems that can generate and preserve quantum correlation, such as rare-earth-doped crystals [28,29]. Specifically, one crystal can be trapped and released to generate light–crystal correlation. The other crystal, fixed on platform, acts as the quantum memorizer. Acceleration sensitivity also depends on the phase-sensitive particle number and memory time.

APPENDIX A: GENERATION OF QUANTUM CORRELATION

Step 1 and step 3 in the accelerometer scheme are SRS processes. The atomic levels and optical frequencies are shown in Fig. 1. In the SRS process, a pair of lower-level meta-stable states is coupled to the Raman pump P_1 (or P_2) and the Stokes field $\hat{a}_1$ (or $\hat{a}_3$) via an upper excited level. After adiabatically eliminating the upper excited level, this is a three-wave mixing process involving the Raman pump field, Stokes field, and a collective atomic pseudo-spin field $\hat{S}_a$. The coupling Hamiltonian is given by [37,38]

$$H = i\hbar\xi\hat{a}^{\dagger}\hat{S}_a^{\dagger} + \text{h.c.}, \tag{A1}$$

where ξ is the coupling coefficient. The time evolution for $\hat{a}$ and $\hat{S}_a$ is given by

$$\hat{a} = G\hat{a}_0 + g\hat{S}_{a_0}^{\dagger}e^{i\theta_P},$$
$$\hat{S}_a = G\hat{S}_{a_0} + g\hat{a}_0^{\dagger}e^{i\theta_P}. \tag{A2}$$

In the case of Raman amplification, G, being the Raman gain, is larger than one, and $g \equiv \sqrt{G^2 - 1}$ with θ_P the phase of Raman pump beam. In the following, we use G_j ($j = 1,2$) to describe the gain of the jth SRS process.

After the first SRS process in a cold ensemble A_1 (see step 1 in Fig. 1), the Stokes light $\hat{a}_1$ and atomic spin wave $\hat{S}_{a_1}^{(1)}$ are generated and written as

$$\hat{a}_1 = G_1\hat{a}_0 + g_1\hat{S}_{a_0}^{(1)\dagger}e^{i\theta_{P_1}}, \quad \hat{S}_{a_1}^{(1)} = G_1\hat{S}_{a_0}^{(1)} + g_1\hat{a}_0^{\dagger}e^{i\theta_{P_1}}, \tag{A3}$$

and they are temporally correlated. This correlation can be demonstrated by calculating the relative intensity variance. After the first SRS has occurred, their intensities are

$$\langle\hat{a}_1^{\dagger}\hat{a}_1\rangle = G_1^2\langle\hat{a}_0^{\dagger}\hat{a}_0\rangle + g_1^2 \simeq G_1^2\langle\hat{a}_0^{\dagger}\hat{a}_0\rangle,$$
$$\langle\hat{S}_{a_1}^{(1)\dagger}\hat{S}_{a_1}^{(1)}\rangle = g_1^2\langle\hat{a}_0^{\dagger}\hat{a}_0\rangle + g_1^2 \simeq (G_1^2 - 1)\langle\hat{a}_0^{\dagger}\hat{a}_0\rangle. \tag{A4}$$

The number difference operator $\hat{a}_1^{\dagger}\hat{a}_1 - \hat{S}_{a_1}^{(1)\dagger}\hat{S}_{a_1}^{(1)}$ describes the relative intensity fluctuations. After the first SRS process, the relative intensity fluctuation is given by

$$\text{Var}(\hat{a}_1^{\dagger}\hat{a}_1 - \hat{S}_{a_1}^{(1)\dagger}\hat{S}_{a_1}^{(1)}) = \text{Var}(\hat{a}_0^{\dagger}\hat{a}_0) = \langle\hat{a}_0^{\dagger}\hat{a}_0\rangle, \tag{A5}$$

where we consider an SNL input light $\text{Var}(\hat{a}_0^{\dagger}\hat{a}_0) = \langle\hat{a}_0^{\dagger}\hat{a}_0\rangle$. The SNL is then the shot noise that would be expected for a differential measurement made with equivalent total power. For the output fields, the SNL is $\langle\hat{a}_1^{\dagger}\hat{a}_1 + \hat{S}_{a_1}^{(1)\dagger}\hat{S}_{a_1}^{(1)}\rangle = (2G_1^2 - 1)\langle\hat{a}_0^{\dagger}\hat{a}_0\rangle$.

Provided the input beams were originally SNL, this SRS process enables sub-shot noise measurements to be made. This is quantified by the "degree of squeezing" (DOS), which is the ratio of the variance of squeezed beams to the variance at the SNL, namely,

$$\text{DOS} = \frac{\langle\hat{a}_0^{\dagger}\hat{a}_0\rangle}{(2G_1^2 - 1)\langle\hat{a}_0^{\dagger}\hat{a}_0\rangle} = \frac{1}{2G_1^2 - 1}. \tag{A6}$$

The variances in the number operator of one beam alone under SRS are

$$\text{Var}(\hat{a}_1^{\dagger}\hat{a}_1) = G_1^4\text{Var}(\hat{a}_0^{\dagger}\hat{a}_0) + G_1^2(G_1^2 - 1)\langle\hat{a}_0^{\dagger}\hat{a}_0\rangle$$
$$= G_1^2(2G_1^2 - 1)\langle\hat{a}_0^{\dagger}\hat{a}_0\rangle, \tag{A7}$$

and

$$\text{Var}(\hat{S}_{a_1}^{(1)\dagger}\hat{S}_{a_1}^{(1)}) = (G_1^2 - 1)^2\text{Var}(\hat{a}_0^{\dagger}\hat{a}_0) + G_1^2(G_1^2 - 1)\langle\hat{a}_0^{\dagger}\hat{a}_0\rangle$$
$$= (G_1^2 - 1)(2G_1^2 - 1)\langle\hat{a}_0^{\dagger}\hat{a}_0\rangle. \tag{A8}$$

Using Eq. (A3), the DOS is $\text{DOS} = 2G_1^2 - 1$. This corresponds to a linear increase in the noise on the two beams as gains are increased.

After SRS, the intensity fluctuation for $\hat{a}_1$ or $\hat{S}_{a_1}^{(1)}$ alone is larger than SNL with $G_1 > 1$. But relative intensity fluctuation $\hat{a}_1^{\dagger}\hat{a}_1 - \hat{S}_{a_1}^{(1)\dagger}\hat{S}_{a_1}^{(1)}$ is smaller than SNL by $2G_1^2 - 1$ times. That is,

$\hat{a}_1$ or $\hat{S}_{a_1}^{(1)}$ is quantum correlated. The second SRS process (see step 3 in Fig. 1) for correlation generation between $\hat{a}_3$ and $\hat{S}_{a_2}^{(1)}$ is similar to the above result.

APPENDIX B: MEMORY PROCESS

The Hamiltonian in the writing process can be written as follows:

$$H = \hbar\chi\hat{a}\hat{S}_a^\dagger + \text{h.c.}, \tag{B1}$$

where χ is the coupling coefficient. Since the pulse time is relatively short, the writing process can be considered approximately lossless. The evolution equations for $\hat{a}$ and $\hat{S}_a$ are

$$\frac{\partial}{\partial t}\hat{a} = -i\chi^*\hat{S}_a, \qquad \frac{\partial}{\partial t}\hat{S}_a = -i\chi\hat{a}, \tag{B2}$$

where χ is the coefficient associated with the write beam. Considering the detuning and the Doppler effect due to atomic center of mass motion with velocity $\mathbf{v}$, the evolution of $\hat{S}_a$, coupling to field $\hat{a}$, can be described by the matrix equation

$$\frac{\partial}{\partial t}\begin{pmatrix} \hat{a} \\ \hat{S}_a \end{pmatrix} = -i\begin{pmatrix} 0 & \chi^* \\ \chi & \alpha_W \end{pmatrix}\begin{pmatrix} \hat{a} \\ \hat{S}_a \end{pmatrix}, \tag{B3}$$

where $\alpha_W = |\Omega_W|^2/\Delta - \delta + \Delta\mathbf{k}_W \cdot \mathbf{v}$, Ω_W is the Rabi frequency of the write field W, Δ is single-photon detuning, δ is two-photon detuning, and $\Delta\mathbf{k}_W = \mathbf{k}_W - \mathbf{k}_S$ is the wave vector difference of W and $\hat{a}_1$. By substituting the following initial conditions into coupling Eq. (B3):

$$\hat{a}(t=0) = \hat{a}_1 e^{i\varphi}, \varphi = k_s L_0,$$
$$\hat{S}_a(t=0) = \hat{S}_{a_0}^{(2)}, \tag{B4}$$

we obtain the following solutions:

$$\hat{S}_{a_1}^{(2)} = e^{-i\alpha_W t_W/2}\left\{ \left[-i\frac{2|\chi|}{\beta_W}e^{i\theta_W}\sin\left(\frac{\beta_W}{2}t_W\right) \right]\hat{a}_1 e^{i\varphi} \right.$$
$$\left. + \left[-i\frac{\alpha_W}{\beta_W}\sin\left(\frac{\beta_W}{2}t_W\right) + \cos\left(\frac{\beta_W}{2}t_W\right) \right]\hat{S}_{a_0}^{(2)} \right\},$$

$$\hat{a}_L = e^{-i\alpha_W t_W/2}\left\{ \left[-i\frac{2|\chi|}{\beta_W}e^{-i\theta_W}\sin\left(\frac{\beta_W}{2}t_W\right) \right]\hat{S}_{a_0}^{(2)} \right.$$
$$\left. + \left[i\frac{\alpha_W}{\beta_W}\sin\left(\frac{\beta_W}{2}t_W\right) + \cos\left(\frac{\beta_W}{2}t_W\right) \right]\hat{a}_1 e^{i\varphi} \right\}, \tag{B5}$$

where $\theta_W = \arg(A_W)$ is the write beam phase, $\beta_W = \sqrt{\alpha_W^2 + 4|\chi|^2}$, and $\hat{a}_L$ is the Stokes signal leaked out from atomic vapor cell A_2 during imperfect storage. It is easy to find that

$$\left| -i\frac{2|\chi|}{\beta_W}e^{i\theta_W}\sin\left(\frac{\beta_W}{2}t_W\right) \right|^2$$
$$+ \left| -i\frac{\alpha_W}{\beta_W}\sin\left(\frac{\beta_W}{2}t_W\right) + \cos\left(\frac{\beta_W}{2}t_W\right) \right|^2 = 1. \tag{B6}$$

We can set $\sqrt{\eta_W} = \frac{2|\chi|}{\beta_W}\sin(\frac{\beta_W}{2}t_W)$, $\sqrt{1-\eta_W}e^{i\theta_{W_0}} = -i\frac{\alpha_W}{\beta_W}\sin(\frac{\beta_W}{2}t_W) + \cos(\frac{\beta_W}{2}t_W)$, and η_W represents the write efficiency. θ_{W_0} is the phase induced by the writing process, which can be considered as a fixed value. Then,

$$\hat{S}_{a_1}^{(2)} = e^{-i\alpha_W t_W/2}[-i\sqrt{\eta_W}e^{i\theta_W}\hat{a}_1 e^{i\varphi} + e^{i\theta_{W_0}}\sqrt{1-\eta_W}\hat{S}_{a_0}^{(2)}],$$
$$\hat{a}_L = e^{-i\alpha_W t_W/2}[-i\sqrt{\eta_W}e^{-i\theta_W}\hat{S}_{a_0}^{(2)} + e^{-i\theta_{W_0}}\sqrt{1-\eta_W}\hat{a}_1 e^{i\varphi}]. \tag{B7}$$

During the storage period t_M, atomic vapor is subject to acceleration $\mathbf{a}$, which causes a change of atomic center of mass velocity $\mathbf{v} \to \mathbf{v} + \mathbf{a}t$, and to the decoherence with decay rate Γ_2 due to atomic collisions. These result in the evolution of the spin wave $\hat{S}_{a_1}^{(2)}$ into $\hat{S}_{a_2}^{(2)} = \hat{S}_{a_1}^{(2)}e^{-\Gamma_2 t_M}e^{-i\phi(t_M)} + \hat{F}^{(2)}$, where $\phi(t_M) = \int_0^{t_M}\Delta\mathbf{k}_W \cdot \mathbf{v}\,dt = \Delta\mathbf{k}_W \cdot \mathbf{v}t_M + \Delta\mathbf{k}_W \cdot \mathbf{a}t_M^2/2$, and $\hat{F}^{(2)}$ is the Langevin operator describing the noise, and satisfies $[\hat{F}^{(2)}, \hat{F}^{(2)\dagger}] = 1 - e^{-2\Gamma_2 t_M}$ [24].

APPENDIX C: READOUT PROCESS

After storage, the spin wave is read out by a read beam with Rabi frequency Ω_R, and the readout field propagating into cold ensemble A_1 has the form

$$\hat{a}_2 = e^{-i\alpha_R t_R/2}e^{ik_s(L_0 + \Delta L)}(-i\sqrt{\eta_R}e^{-i\theta_R}\hat{S}_{a_2}^{(2)} + e^{-i\theta_{R_0}}\sqrt{1-\eta_R}\hat{b}), \tag{C1}$$

where L_0 is the distance between cold ensemble A_1 and atomic vapor cell A_2 before MOT is turned off, ΔL is the acceleration-induced distance change, $\alpha_R = \frac{|\Omega_R|^2}{\Delta} - \delta + \Delta\mathbf{k}_R \cdot \mathbf{v}$, $\beta_R = \sqrt{\alpha_R^2 + 4|\chi|^2}$, θ_R is the read beam phase, t_R is the reading time, and $\Delta\mathbf{k}_R = \mathbf{k}_R - \mathbf{k}_S$ is the wave vector difference of read field R and $\hat{a}_2$. We set $\sqrt{\eta_R} = \frac{2|\chi|}{\beta_R}\sin(\frac{\beta_R}{2}t_R)$, $\sqrt{1-\eta_R}e^{i\theta_{R_0}} = -i\frac{\alpha_R}{\beta_R}\sin(\frac{\beta_R}{2}t_R) + \cos(\frac{\beta_R}{2}t_R)$, with η_R the read efficiency. θ_{R_0} is the phase induced by the readout process, which can be considered as a fixed value.

Finally, $\hat{a}_2$ can be expressed as the following via the input light field $\hat{a}_1$:

$$\hat{a}_2 = e^{-i\alpha_R t_R/2}e^{ik_s(L_0 + \Delta L)}(-i\sqrt{\eta_R}e^{-i\theta_R}\hat{S}_{a_2}^{(2)} + e^{-i\theta_{R_0}}\sqrt{1-\eta_R}\hat{b})$$
$$= e^{-i\alpha_R t_R/2}e^{ik_s(L_0 + \Delta L)}[-i\sqrt{\eta_R}e^{-i\theta_R}(\hat{S}_{a_1}^{(2)}e^{-\Gamma_2 t_M}e^{-i\phi(t_M)} + \hat{F}^{(2)})$$
$$+ e^{-i\theta_{R_0}}\sqrt{1-\eta_R}\hat{b}]$$
$$= e^{-i\alpha_R t_R/2}e^{ik_s(L_0 + \Delta L)}\{-i\sqrt{\eta_R}e^{-i\theta_R}[e^{-i\alpha_W t_W/2}$$
$$\times (-i\sqrt{\eta_W}\hat{a}_1 e^{i\theta_W}e^{ik_s L_0} + e^{i\theta_0}\sqrt{1-\eta_W}\hat{S}_{a_0}^{(2)})$$
$$\times e^{-\Gamma_2 t_M}e^{-i\phi(t_M)} + \hat{F}^{(2)}] + e^{-i\theta_{R_0}}\sqrt{1-\eta_R}\hat{b}\}$$
$$= -e^{-i[(\alpha_W t_W + \alpha_R t_R)/2 + \phi(t_M) - k_s(2L_0 + \Delta L)]}$$
$$\times e^{i(\theta_W - \theta_R)}\sqrt{\eta_W \eta_R}e^{-\Gamma_2 t_M}\hat{a}_1 + \hat{D}, \tag{C2}$$

where the total noise operator $\hat{D} \equiv e^{-i(\alpha_W t_W + \alpha_R t_R)/2}$. $e^{ik_s(L_0 + \Delta L)}[-i\sqrt{\eta_R(1-\eta_W)}e^{i(\theta_{W_0} - \theta_R)}e^{-\Gamma_2 t_M}e^{-i\phi(t_M)}\hat{S}_{a_0}^{(2)} - i\sqrt{\eta_R} \cdot e^{-i\theta_R}e^{i\alpha_W t_W/2}\hat{F}^{(2)} + e^{-i\theta_{R_0}}\sqrt{1-\eta_R}e^{i\alpha_W t_W/2}\hat{b}]$, $\hat{S}_{a_0}^{(2)}$ and $\hat{b}$ are vacuum inputs of the spin wave and light field, respectively, with operator $\hat{b}$ satisfying the bosonic commutation relation $[\hat{b}, \hat{b}^\dagger] = 1$. Here, the spin wave $\hat{S}_{a_0}^{(2)}$ can approximately be treated as a bosonic field $[\hat{S}_{a_0}^{(2)}, \hat{S}_{a_0}^{(2)\dagger}] \approx 1$ because the number of atomic spin excitations is much smaller than the total atomic number. The commutation relation of operator $\hat{D}$ is

$$[\hat{D}, \hat{D}^\dagger] = 1 - \eta_W \eta_R e^{-2\Gamma_2 t_M}, \tag{C3}$$

and for convenience, operator $\hat{D}$ can be normalized to $\hat{D} = \sqrt{1 - \eta_W \eta_R e^{-2\Gamma_2 t_M}} \hat{V}$, with $\hat{V}$ being the effective vacuum field and satisfying $[\hat{V}, \hat{V}^\dagger] = 1$.

In addition, without loss of generality, assuming that $\Omega_W = \Omega_R$, $t_W = t_R$, $\Delta\mathbf{k}_R = -\Delta\mathbf{k}_W$, and considering $\mathbf{v} \to \mathbf{v} + \mathbf{a}t_M$ at the readout time, the phase term in Eq. (C2) is

$$(\alpha_W t_W + \alpha_R t_R)/2 + \phi(t_M) - k_s(2L_0 + \Delta L)$$
$$= (\alpha_W + \alpha_R)t_W/2 + \phi(t_M) - k_s(2L_0 + \Delta L)$$
$$= \left(\frac{|\Omega_W|^2}{\Delta} - \delta\right)t_W + \Delta kat_M(t_M - t_W)/2 + \Delta\mathbf{k}_W \cdot \mathbf{v}t_M$$
$$- k_s(2L_0 + \Delta L)$$
$$\equiv \Delta\varphi_a + \Delta\varphi_v - \varphi_0, \qquad \text{(C4)}$$

where Δk is the projection of $\Delta\mathbf{k}_W$ along $\mathbf{a}$, and $\varphi_0 \equiv -(\frac{|\Omega_W|^2}{\Delta} - \delta)t_W + 2k_s L_0$, $\Delta\varphi_v \equiv \Delta\mathbf{k}_W \cdot \mathbf{v}t_M$, $\Delta\varphi_a \equiv \Delta kat_M(t_M - t_W)/2 - k_s(\Delta L)$. φ_0 is a determined overall phase offset accumulated by the Stark effect, two-photon detuning, and propagation distance L_0. The velocity-dependent phase shift $\Delta\varphi_v = \Delta\mathbf{k}_W \cdot \mathbf{v}t_M$ induces decoherence due to the dephasing process from atomic thermal motion. $\Delta\varphi_a$ is the acceleration-dependent phase shift. The reading and writing beams originate from the same laser, and their phases satisfy $\theta_W - \theta_R = 0$. Finally, defining $\eta = \eta_W \eta_R$ Stokes $\hat{a}_2$ can be simplified as

$$\hat{a}_2 = -\sqrt{\eta}e^{-i(\Delta\varphi_a + \Delta\varphi_v - \varphi_0)}e^{-\Gamma_2 t_M}\hat{a}_1 + \sqrt{1 - \eta e^{-2\Gamma_2 t_M}}\hat{V}. \quad \text{(C5)}$$

φ_0 can be set to zero by adjusting the initial setup of the system since it is independent of the measured acceleration $\mathbf{a}$. The acceleration rate can be measured by reading out the phase shift $\Delta\varphi_a$ through atom–light interference between the readout field $\hat{a}_2$ returning to cold ensemble A_1 and atomic spin wave $\hat{S}_{a_1}^{(1)}$ remaining in A_1.

APPENDIX D: ATOM–LIGHT INTERFERENCE

First, we analyze the time evolution of the spin wave $\hat{S}_{a_1}^{(1)}$ remaining in cold ensemble A_1 during the memory process. Spin wave $\hat{S}_{a_1}^{(1)}$ evolves to $\hat{S}_{a_2}^{(1)}$ with decay rate Γ_1, which is given as

$$\hat{S}_{a_2}^{(1)} = \hat{S}_{a_1}^{(1)} e^{-\Gamma_1 t_M} e^{i\delta t_M} e^{-i\Delta\mathbf{k}_{P1} \cdot \mathbf{v}t_M} + \hat{F}^{(1)}, \qquad \text{(D1)}$$

where $\Delta\mathbf{k}_{P1} = \mathbf{k}_{P1} - \mathbf{k}_S$ is the wave vector difference of pump field P_1 and $\hat{a}_1$, and $\hat{F}^{(1)}$ is the quantum statistical Langevin operator, which reflects the collision-induced fluctuation and satisfies $[\hat{F}^{(1)}, \hat{F}^{(1)\dagger}] = 1 - e^{-2\Gamma_1 t_M}$. The decay rate Γ_1 represents the decoherence effect due to atomic collisions and flying off a laser beam. For a general cold atomic ensemble, the root mean square velocity is ∼ several cm/s, and the diffusion of cold atoms is ∼1.0 mm after a memory time of 10 ms. The whole atomic ensemble will drop 0.5 mm in gravity direction after 10 ms. The spot expansion and dropping of the cold atomic ensemble can result in a mismatch between returned light and atomic spin wave. However, these two effects can be solved using laser beam expansion and light path adjustment in the experiment. The dephasing induced by atomic motion is very slow. Thus, on the time scale, $t_M \sim$ ms, dephasing can be safely ignored. Finally, considering the two-photon resonance in this work, $\hat{S}_{a_2}^{(1)} \simeq \hat{S}_{a_1}^{(1)} e^{-\Gamma_1 t_M} + \hat{F}^{(1)}$.

Light fields $\hat{a}_2$ and $\hat{S}_{a_2}^{(1)}$ interact with each other in cold ensemble A_1, and generate Stokes $\hat{a}_{\text{out}}$ and atomic spin wave $\hat{S}_{a_{\text{out}}}^{(1)}$ by a second Raman scattering P_2. The input–output relation of the second SRS can be written as

$$\hat{a}_{\text{out}} = G_2 \hat{a}_2 + g_2 \hat{S}_{a_2}^{(1)\dagger} e^{i\theta_{P_2}}. \qquad \text{(D2)}$$

Raman beams P_1 and P_2 originate from the same laser, and their phases satisfy $\theta_{P_1} - \theta_{P_2} = 0$. The combination of $\hat{a}_2$ and $\hat{S}_{a_2}^{(1)\dagger}$, output field $\hat{a}_{\text{out}}$ from ensemble A_1, is given by

$$\hat{a}_{\text{out}} = \varsigma_1 \hat{a}_0 + \varsigma_2 \hat{S}_{a_0}^{(1)\dagger} + \varsigma_3 \hat{V} + \varsigma_4 \hat{f}^\dagger, \qquad \text{(D3)}$$

where the normalized noise operator $\hat{f} = \hat{F}^{(1)}/\sqrt{1 - e^{-2\Gamma_1 t_M}}$, with $[\hat{f}, \hat{f}^\dagger] = 1$, and

$$\varsigma_1 = g_1 g_2 e^{-\Gamma_1 t_M} - G_1 G_2 \sqrt{\eta} e^{-\Gamma_2 t_M} e^{i(\Delta\varphi_a + \Delta\varphi_v)},$$
$$\varsigma_2 = e^{i\theta_{P_2}}[G_1 g_2 e^{-\Gamma_1 t_M} - g_1 G_2 \sqrt{\eta} e^{-\Gamma_2 t_M} e^{i(\Delta\varphi_a + \Delta\varphi_v)}],$$
$$\varsigma_3 = G_2 \sqrt{1 - \eta e^{-2\Gamma_2 t_M}}, \qquad \varsigma_4 = g_2 e^{i\theta_{P_2}} \sqrt{1 - e^{-2\Gamma_1 t_M}}.$$

The acceleration-dependent phase shift $\Delta\varphi_a \equiv \Delta kat_M(t_M - t_W)/2 - k_s(\Delta L)$, with $\Delta L = \frac{1}{2}a(t_1 + t_2 + t_M)^2$, where t_1 and t_2 are the flying times of Stokes light between A_1 and A_2 forth and back, respectively. Normally, $k_s \gg |\Delta k|$ and $t_M \gg t_{W,R} \gg t_{1,2}$, i.e., $\Delta\varphi_a \simeq -k_s at_M^2/2$. The phase shift $\Delta\varphi_a$ can be measured through the readout field $\hat{a}_{\text{out}}$, which is affected by optical loss η and atomic decoherence including $e^{-2\Gamma_1 t_M}$, $e^{-2\Gamma_2 t_M}$ induced by collision, and $e^{i\Delta\varphi_v}$ induced by atomic thermal motion.

APPENDIX E: ACCELERATION SENSITIVITY USING HOMODYNE DETECTION

All optical devices including the vacuum chamber and memory element are fixed onto a mobile platform. When MOT is turned on, cold ensemble A_1 and atomic vapor cell A_2 move together with the platform. The distance L between two atomic systems is fixed as L_0 at any velocity or acceleration of the platform. When MOT is turned off, A_1 is free-falling in vacuum, acting as a static frame reference, and A_2 remains moving with the platform at acceleration a. $L = L_0 + \Delta L$ changes with the acceleration, where ΔL is the displacement due to acceleration a. $\Delta L = \Delta v_0 T + \frac{1}{2}aT^2$, Δv_0 is initial relative velocity of A_1 and A_2, and T is the free-evolution time duration after the first Raman scattering process and before the second one. Δv_0 is zero because the velocities of two atomic systems are the same before MOT is turned off. T is independent of acceleration a and the velocity of the platform. ΔL causes the phase shift.

The phase shift induced by acceleration can be measured via atom–light quantum interference. It is noted that the scheme can measure acceleration only in the direction of the seed and pump fields passing the cold ensemble, and its sensitivity is [20,24]

$$\Delta a = \frac{\lambda_s}{\pi t_M^2} \frac{\langle(\Delta\hat{O})^2\rangle^{1/2}}{|\partial\hat{O}/\partial\varphi|}, \qquad \text{(E1)}$$

where $\hat{O}$ is the measured operator related to the phase shift.

We use HD to measure the interference output field $\hat{a}_{\text{out}}$, where the measured operator is the quadrature operator $X = \hat{a}_{\text{out}} e^{i\theta_l} + \hat{a}_{\text{out}}^\dagger e^{-i\theta_l}$, where θ_l is the phase of the local oscillator.

As $\hat{a}_0$ is coherent light $|\alpha\rangle$ ($\alpha = |\alpha|e^{i\theta_\alpha}$), according to $\hat{a}_{\text{out}}$ of Eq. (D3), the slope is given by

$$\left| \frac{\partial \langle \hat{X} \rangle}{\partial (\Delta\varphi_a)} \right|$$
$$= 2 \exp\left(-\frac{t_M^2}{\tau^2}\right) \sqrt{\eta} e^{-\Gamma_2 t_M} G_1 G_2 \sqrt{N_0} \sin(\theta_l + \theta_\alpha - \Delta\varphi_a).$$
$$\text{(E2)}$$

The dephasing term $\exp(-t_M^2/\tau^2)$ comes from the velocity-dependent phase shift $\Delta\varphi_v$, where $\tau = \sqrt{2}/(\Delta k_W)\bar{v}_{\text{rms}}$ with the root mean square velocity of atoms $\bar{v}_{\text{rms}} = \sqrt{k_B T/m}$ [39,40]. When $\theta_l + \theta_\alpha - \Delta\varphi_a = \pi/2$, the slope $|\partial\langle\hat{X}\rangle/\partial(\Delta\varphi_a)|$ reaches its maximum.

The variance is

$$\langle \Delta^2 \hat{X} \rangle = |\varsigma_1|^2 + |\varsigma_2|^2 + |\varsigma_3|^2 + |\varsigma_4|^2, \quad \text{(E3)}$$

where coefficients

$$|\varsigma_1| = \left| - e^{-i\Delta\varphi_a} \exp\left(-\frac{t_M^2}{\tau^2}\right) e^{-\Gamma_2 t_M} G_1 G_2 + e^{-\Gamma_1 t_M} g_1 g_2 \right|,$$

$$|\varsigma_2| = \left| G_1 g_2 e^{-\Gamma_1 t_M} - G_2 g_1 e^{-i\Delta\varphi_a} \exp\left(-\frac{t_M^2}{\tau^2}\right) \sqrt{\eta} e^{-\Gamma_2 t_M} \right|,$$

$$|\varsigma_3| = G_2 \sqrt{1 - \eta e^{-2\Gamma_2 t_M}}, |\varsigma_4| = g_2 \sqrt{1 - e^{-2\Gamma_1 t_M}}, \quad \text{(E4)}$$

reach their minimum at $\Delta\varphi_a \sim 0$, giving the minimal variance $\langle \Delta^2 \hat{X} \rangle$.

The decay terms $e^{-\Gamma_1 t_M}$, $e^{-\Gamma_2 t_M}$ and the dephasing term $\exp(-t_M^2/\tau^2)$ degrade the sensitivity of acceleration measurement. The decoherence time $\tau = \sqrt{2}/(\Delta k_W \bar{v}_{\text{rms}})$ depends on the Δk_W and root mean square velocity $\bar{v}_{\text{rms}}$ of atomic thermal motion. To reduce the effect of Doppler dephasing, one can employ laser-cooled atomic gas with low $\bar{v}_{\text{rms}}$ or use near-degenerate sublevels to achieve very small Δk_W. However, in our design, the second cell A_2 with atoms in it is assumed as a whole to be attached to the platform, sensing the acceleration. For this purpose, the atomic thermal motion in the cell must be rapid enough to remain in thermal equilibrium with the cell walls under acceleration. In this sense, a vapor cell with buffer gas is essential, ruling out the usage of laser-cooled atomic gas. The collision between buffer gas and atoms almost has no effect on hyperfine coherence in principle. In a reported paper, ground-state coherence can be preserved for up to 10^8 collisions with buffer gas [31]. The atoms of buffer gas can separate the original atoms and decrease the collision between them. Therefore, the value of the decay rate Γ_2 in Fig. 3 is small [32]. For a negligible dephasing effect, e.g., $t_M/\tau = t_M(\Delta k_W)\bar{v}_{\text{rms}}/\sqrt{2} \sim 0.1$, we work out $\Delta k_W \sim 0.1 \times \sqrt{2}/(\bar{v}_{\text{rms}} t_M)$. For a typical room-temperature vapor cell with $\bar{v}_{\text{rms}} \sim 300$ m/s and giving $t_M \sim 10$ ms, $\Delta k_W \sim 2.3 \times 2\pi$ MHz/c. This can experimentally be realized by choosing Zeeman sublevels with frequency differences near MHz for two-photon transitions [36].

Based on the arguments above, the acceleration sensitivity is

$$\Delta a = \frac{\lambda_s}{\pi t_M^2} \frac{\sqrt{\langle \Delta^2 \hat{X} \rangle}}{\left| \frac{\partial\langle\hat{X}\rangle}{\partial(\Delta\varphi_a)} \right|} = \frac{1}{Q_e} \Delta a_{\text{SNL}}, \quad \text{(E5)}$$

where $\Delta a_{\text{SNL}} \approx \frac{2\lambda_s}{\sqrt{G_1^2 + g_1^2 N_0 t_M^2}}$ is the SNL for the accelerometer, and Q_e is the quantum enhancement factor:

$$Q_e = \frac{2G_1 G_2}{\sqrt{G_1^2 + g_1^2}} \frac{\sqrt{\eta} e^{-\Gamma_2 t_M}}{\sqrt{\sum_{n=1}^{4} |\varsigma_n^0|^2}}, \quad \text{(E6)}$$

where ς_n^0 ($n = 1, ..., 4$) are the values of ς_n when the MQA is operated at the dark fringe with a small phase shift.

Disclosures. The authors declare no conflicts of interest.

Data Availability. Data underlying the results presented in this paper are not publicly available at this time but may be obtained from the authors upon reasonable request.

REFERENCES

1. P. S. de Brito Andre and H. Varum, *Accelerometers: Principles, Structure and Applications* (Nova Science, 2013).
2. M. Bao, *Micro Mechanical Transducers: Pressure Sensors, Accelerometers and Gyroscopes* (Elsevier, 2000).
3. C.-W. Tan and S. Park, "Design of accelerometer-based inertial navigation systems," IEEE Trans. Instrum. Meas. **54**, 2520–2530 (2005).
4. D. Jiang, W. Zhang, and F. Li, "All-metal optical fiber accelerometer with low transverse sensitivity for seismic monitoring," IEEE Sens. J. **13**, 4556–4560 (2013).
5. C. Acar and A. M. Shkel, "Experimental evaluation and comparative analysis of commercial variable-capacitance MEMS accelerometers," J. Micromech. Microeng. **13**, 634–645 (2003).
6. Y. Dong, P. Zwahlen, A. M. Nguyen, R. Frosio, and F. Rudolf, "Ultra-high precision MEMS accelerometer," in *16th International Solid-State Sensors, Actuators and Microsystems Conference* (2011), pp. 695–698.
7. S. Tadigadapa and K. Mateti, "Piezoelectric MEMS sensors: state-of-the-art and perspectives," Meas. Sci. Technol. **20**, 092001 (2009).
8. C. Liu, A. M. Barzilai, J. K. Reynolds, A. Partridge, T. W. Kenny, J. D. Grade, and H. K. Rockstad, "Characterization of a high-sensitivity micromachined tunneling accelerometer with micro-g resolution," J. Microelectromech. Syst. **7**, 235–244 (1998).
9. R. Mukherjee, J. Basu, P. Mandal, and P. K. Guha, "A review of micromachined thermal accelerometers," J. Micromech. Microeng. **27**, 123002 (2017).
10. U. Krishnamoorthy, R. H. Olsson III, G. R. Bogart, M. S. Baker, D. W. Carr, T. P. Swiler, and P. J. Clews, "Inplane MEMS-based nano-g accelerometer with sub-wavelength optical resonant sensor," Sens. Actuators A Phys. **145**, 283–290 (2008).
11. K. Zandi, B. Wong, J. Zou, R. V. Kruzelecky, W. Jamroz, and Y. Peter, "In-plane silicon-on-insulator optical MEMS accelerometer using waveguide Fabry-Perot microcavity with silicon/air Bragg mirror," in *IEEE 23rd International Conference on Micro Electro Mechanical Systems (MEMS)* (IEEE, 2010), pp. 839–842.
12. W. Noell, "Applications of SOI-based optical MEMS," IEEE J. Sel. Top. Quantum Electron. **8**, 148–154 (2002).

13. T. A. Berkoff and A. D. Kersey, "Experimental demonstration of a fiber Bragg grating accelerometer," IEEE Photon. Technol. Lett. **8**, 1677–1679 (1996).

14. A. G. Krause, M. Winger, T. D. Blasius, Q. Lin, and O. Painter, "A microchip optomechanical accelerometer," Nat. Photonics **6**, 768–772 (2012).

15. Y. Yang, X. Li, K. Kou, and L. Zhang, "Optical accelerometer design based on laser self-mixing interference," Proc. SPIE **9369**, 93690R (2015).

16. Y. L. Li and P. F. Barker, "Characterization and testing of a micro-g whispering gallery mode optomechanical accelerometer," J. Lightwave Technol. **36**, 3919–3926 (2018).

17. N. Lagakos, T. Litovitz, P. Macedo, R. Mohr, and R. Meister, "Multimode optical fiber displacement sensor," Appl. Opt. **20**, 167–168 (1981).

18. S. Chen and H. Xu, "Design analysis of a high-Q micromechanical capacitive accelerometer system," IEICE Electron. Express **14**, 20170410 (2017).

19. M. D. LeHaye, O. Buu, B. Camarota, and K. C. Schwab, "Approaching the quantum limit of a nanomechanical resonator," Science **304**, 74–77 (2004).

20. J. P. Dowling, "Quantum optical metrology-the lowdown on high-N00N states," Contemp. Phys. **49**, 125–143 (2008).

21. P. Qian, Z. Gu, R. Cao, R. Wen, Z. Y. Ou, J. F. Chen, and W. Zhang, "Temporal purity and quantum interference of single photons from two independent cold atomic ensembles," Phys. Rev. Lett. **117**, 013602 (2016).

22. B. Chen, C. Qiu, S. Chen, J. Guo, L. Q. Chen, Z. Y. Ou, and W. Zhang, "Atom-light hybrid interferometer," Phys. Rev. Lett. **115**, 043602 (2015).

23. X. Feng, Z. Yu, B. Chen, S. Chen, Y. Wu, D. Fan, C.-H. Yuan, L. Q. Chen, Z. Y. Ou, and W. Zhang, "Reducing the mode-mismatch noises in atom-light interactions via optimization of the temporal waveform," Photon. Res. **8**, 1697–1702 (2020).

24. Z.-D. Chen, C.-H. Yuan, H.-M. Ma, D. Li, L. Q. Chen, Z. Y. Ou, and W. Zhang, "Effects of losses in the atom-light hybrid SU(1,1) interferometer," Opt. Express **24**, 17766–17778 (2016).

25. C. Liu, Z. Dutton, C. H. Behroozi, and L. V. Hau, "Observation of coherent optical information storage in an atomic medium using halted light pulses," Nature **409**, 490–493 (2001).

26. M. Hosseini, B. M. Sparkes, G. Campbell, P. K. Lam, and B. C. Buchler, "High efficiency coherent optical memory with warm rubidium vapour," Nat. Commun. **2**, 174 (2011).

27. J. Guo, X. Feng, P. Yang, Z. Yu, L. Q. Chen, C.-H. Yuan, and W. Zhang, "High-performance Raman quantum memory with optimal control in room temperature atoms," Nat. Commun. **10**, 148 (2019).

28. Y. Ma, Y.-Z. Ma, Z.-Q. Zhou, C.-F. Li, and G.-C. Guo, "One-hour coherent optical storage in an atomic frequency comb memory," Nat. Commun. **12**, 2381 (2021).

29. M. Zhong, M. P. Hedges, R. L. Ahlefeldt, J. G. Bartholomew, S. E. Beavan, S. M. Wittig, J. J. Longdell, and M. J. Sellars, "Optically addressable nuclear spins in a solid with a six-hour coherence time," Nature **517**, 177–180 (2015).

30. C. H. van der Wal, M. D. Eisaman, A. André, R. L. Walsworth, D. F. Phillips, A. S. Zibrov, and M. D. Lukin, "Atomic memory for correlated photon states," Science **301**, 196–200 (2003).

31. W. Happer, "Optical pumping," Rev. Mod. Phys. **44**, 169–249 (1972).

32. S. Manz, T. Fernholz, J. Schmiedmayer, and J.-W. Pan, "Collisional decoherence during writing and reading quantum states," Phys. Rev. A **75**, 040101 (2007).

33. S. Zhang, J. F. Chen, C. Liu, S. Zhou, M. M. T. Loy, G. K. L. Wong, and S. Du, "A dark-line two-dimensional magneto optical trap of ^{85}Rb atoms with high optical depth," Rev. Sci. Instrum. **83**, 073102 (2012).

34. A. G. Radnaev, Y. O. Dudin, R. Zhao, H. H. Jen, S. D. Jenkins, A. Kuzmich, and T. A. B. Kennedy, "A quantum memory with telecom-wavelength conversion," Nat. Phys. **6**, 894–899 (2010).

35. X.-H. Bao, A. Reingruber, P. Dietrich, J. Rui, A. Duck, T. Strasse, L. Li, N.-L. Liu, B. Zhao, and J.-W. Pan, "Efficient and long-lived quantum memory with cold atoms inside a ring cavity," Nat. Phys. **8**, 517–521 (2012).

36. O. Katz and O. Firstenberg, "Light storage for one second in room-temperature alkali vapor," Nat. Commun. **9**, 2074 (2018).

37. L.-M. Duan, M. D. Lukin, J. I. Cirac, and P. Zoller, "Long-distance quantum communication with atomic ensembles and linear optics," Nature **414**, 413–418 (2001).

38. K. Hammerer, A. S. Sorensen, and E. S. Polzik, "Quantum interface between light and atomic ensembles," Rev. Mod. Phys. **82**, 1041 (2010).

39. Y. Yoshikawa, Y. Torii, and T. Kuga, "Superradiant light scattering from thermal atomic vapors," Phys. Rev. Lett. **94**, 083602 (2005).

40. B. Zhao, Y. A. Chen, X. H. Bao, T. Strassel, C. S. Chuu, X. M. Jin, J. Schmiedmayer, Z. S. Yuan, S. Chen, and J. W. Pan, "A millisecond quantum memory for scalable quantum networks," Nat. Phys. **5**, 95–99 (2009).